ACS APPLIED MATERIALS & INTERFACES

Research Article

www.acsami.org

Influence of Functionalization of Nanocontainers on Self-Healing Anticorrosive Coatings

Zhaoliang Zheng,*[,†] Matthias Schenderlein,[‡] Xing Huang,[§] Nick J. Brownbill,[†] Frédéric Blanc,[†] and Dmitry Shchukin[†]

[†]Stephenson Institute for Renewable Energy, Department of Chemistry, University of Liverpool, Crown Street, Liverpool, L69 7ZD, United Kingdom

[‡]Max-Planck Institute of Colloids and Interfaces, 14424, Potsdam, Germany

[§]Fritz-Haber-Institut der MPG, Faradayweg 4-6, 14195, Berlin, Germany

Supporting Information

ABSTRACT: Feedback coating based on pH-induced release of inhibitor from organosilyl-functionalized containers is considered as a compelling candidate to achieve smart self-healing corrosion protection. Four key factors that determine the overall coating performance include (1) the uptake and release capacity of containers, (2) prevention of the premature leakage, (3) compatibility of containers in coating matrix, and (4) cost and procedure simplicity consideration. The critical influence introduced by organosilyl-functionalization of containers is systematically demonstrated by investigating MCM-41 silica nanoparticles modified with ethylenediamine (en), en-4-oxobutanoic acid salt (en-COO^-), and en-triacetate (en-$(COO^-)_3$) with higher and lower organic contents. The properties of the modified silica nanoparticles as containers were mainly characterized by solid-state ^{13}C nuclear magnetic resonance, scanning and transmission electron microscopy, N_2 sorption, thermogravimetric analysis, small-angle X-ray scattering, dynamic light scattering, and UV−vis spectroscopy. Finally, the self-healing ability and anticorrosive performances of hybrid coatings were examined through scanning vibrating electrode technique (SVET) and electrochemical impedance spectroscopy (EIS). We found that en-$(COO^-)_3$-type functionalization with content of only 0.23 mmol/g performed the best as a candidate for establishing pH-induced release system because the resulting capped and loaded (C-L) functionalized silica nanocontainers (FSNs) exhibit high loading (26 wt %) and release (80%) capacities for inhibitor, prevention of premature leakage (less than 2%), good dispersibility in coating matrix, and cost effectiveness.

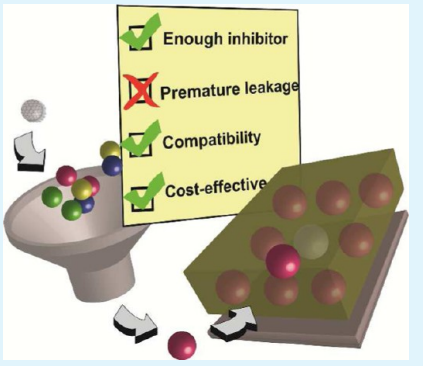

KEYWORDS: *self-healing, anticorrosion, H^+/OH^- dual responsive, feedback coating, nanocontainer, organosilyl-functionalization*

INTRODUCTION

Smart coatings, which are endowed with rapid and sustained response to external impacts (e.g., cracks, pressure, and magnetic and electromagnetic fields) or to changes in the microenvironment (e.g., ion exchange and pH variation) have been considered as compelling candidates for corrosion protection, bioactive species sensor, and antifouling.[1] Among various functionalities of smart coatings, pH-sensitive self-healing encompasses a significant breadth of utility, especially in ceasing the onset and ongoing of corrosion on metal surface. For example, the corrosion inhibitor can be released to the corroded microareas in response to the pH shift[2] at the anodic or cathodic corrosion sites. Incorporating a stimuli-responsive release system in coating matrices enables to overcome the major drawbacks of conventional coatings which provide only a passive protection but lose the protective function when damaged.[3] It is ideal to design and establish such a stimuli-responsive release system that entraps corrosion inhibitor in nanocontainers with a high uptake capacity and releases it only in response to certain stimuli. To find a sensitive release system that suits the application of self-healing anticorrosive coatings, our and other groups[4] have evaluated several options. For instance, polymeric micro/nanosized capsules formed by interfacial polymerization,[5,6] layer-by-layer (LbL) strategy[7,8] or stabilized by inorganic nanoparticles[9,10] can be equipped with pH-sensitive compounds but have drawbacks of severe premature leakage of inhibitor molecules and vulnerability of shell integrity to a long-term deterioration. Mesoporous silica nanoparticles, halloysite clay, and hydroxyapatite microparticles with a high load and release capacity, structure stability and pH-accelerated release of cargo were introduced into self-healing anticorrosive coating matrices.[11−17] However, it still remains an elusive challenge to minimize the premature leakage of cargo from unmodified mesoporous containers.[12]

The functionalization of silica nanocontainers (FSNs) may provide a solution.[18] Zink and Stoddart[19−23] functionalized the

Received: December 24, 2014
Accepted: September 22, 2015

DOI: 10.1021/acsami.5b08028
ACS Appl. Mater. Interfaces XXXX, XXX, XXX−XXX

orifices of mesoporous materials with several pH sensitive supramolecular assemblies to effectively control the release of drug molecules. Muhammad et al.[24] employed amine-functionalization to bind acid-decomposable zinc oxide nanoparticles at the nanopores of MCM-41 nanoparticles. The nanovalves inhibited premature leakage of doxorubicin but were able to open in an acidic environment. Manzano and Vallet-Regí[25,26] also discussed the influence of surface functionalization, for example, carboxylic acid and amine, on the loading and pH-sensitive release kinetics of drug molecules. For most FSNs reported by now, a satisfactory answer on the following questions is still pending: (1) Is there a sufficient loading and release capacity? (2) Is the premature leakage of inhibitor effectively prevented? (3) Do the containers have good adhesion and compatibility with their host matrix? (4) Can the fabrication procedure be simplified for scalable production and the cost be lowered?

In this work, we address the above issues by properly functionalizing mesoporous silica containers. The nanovalve preparation follows a similar method we recently invented for selective absorbing sensor molecules.[27] The organosilyl modification at the orifice of mesopores enables one to use a much broader selection of nanovalves with more predictable functions. Our emphasis here has been directed to the FSNs supporting best self-healing performance. The resulting cotrolled release system exhibits (1) a relatively high loading (26 wt %) and release capacity (80%), (2) negligible premature leakage below 2%, (3) good dispersibility in host coating matrix, and (4) lower cost as compared with other reported systems. The barrier properties and self-healing ability of the studied smart coatings were evaluated by scanning vibrating electrode technique (SVET) and electrochemical impedance spectroscopy (EIS).

RESULTS AND DISCUSSION

Functionalized MCM-41 Silica Nanoparticles (FSNs). We compare three types of functionalizing moieties that are featured with the same silylpropyl-ethylendiamine (en) main structure but differ in the number of carbonate end groups. We use en, en-(COO^-), and en-(COO^-)$_3$ as the notation of the agents with zero, one, and three carbonate groups (Scheme 1).

Scheme 1. Schematic Procedure for the Functionalization of Native MCM-41[a]

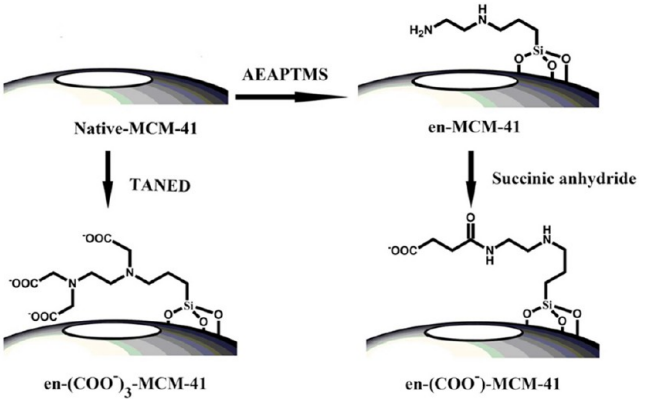

[a]AEAPTMS and TANED represent *N*-(3-trimethoxysilylpropyl)-ethylenediamine and *N*-(trimethoxysilylpropyl)-ethylenediaminetriacetic acid trisodium salt, respectively.

We directly prepared en-MCM-41 and en-(COO^-)$_3$-MCM-41 from the postfunctionalization reaction between silica and *N*-(3-trimethoxysilylpropyl)-ethylenediamine (AEAPTMS) or *N*-(trimethoxysilylpropyl)-ethylenediaminetriacetic acid trisodium salt (TANED) in a reflux of toluene. en-MCM-41 was then treated with succinic anhydride to yield en-4-oxobutanoic acid salt (COO^-) derivatives (Supporting Information). For further comparison, the organic content of FSNs was intentionally tailored at around 0.7 and 0.2 mmol/g (moles of functional moiety per gram of FSNs; Table 1 and Figure S1), respectively.

Successful organosilyl functionalization is revealed in Figure 1 by the ^{13}C Nuclear Magnetic Resonance (NMR) spectra of FSNs 2 (en-MCM-41), FSNs 4 (en-(COO^-)-MCM-41) and FSNs 6 (en-(COO^-)$_3$-MCM-41) obtained under magic angle spinning (MAS) and cross-polarization (CP). The ^{13}C NMR of FSNs 2 (en-MCM-41) showed a characteristic peak at 9 ppm, representative of an $SiCH_2-$ carbon environment (Table S1), and one characteristic alkyl peak ($-SiCH_2CH_2-$) at 22 ppm (Figure 1a). Three additional peaks at higher chemical shifts indicating the $-NH_2CH_2CH_2NHCH_2-$ moieties were also observed at 40 ppm ($-NH_2CH_2-$), 51 ppm ($-NH_2CH_2CH_2NHCH_2-$) and 59 ppm ($-SiCH_2CH_2CH_2-$), confirming the structure of en-MCM-41 on the surface of the silica. FSNs 4 (en-(COO^-)-MCM-41) showed all the same carbon environments as en-MCM-41 (Figure 1b) with four additional peaks coming from the reaction with succinic anhydride. Specifically, the peaks at 180 and 175 ppm represent the carboxylic acid and the amide carbonyl groups, respectively, and two alkyl peaks observed at 47 and 29 ppm (of the two new $-CH_2-$ units) are also observed. We note that the former CH_2 signals integrate higher than the CH_2 peaks in the $-NHCH_2CH_2NHCO-$ group (1.4:1 ratio) and although ^{13}C CP MAS experiments are not a quantitative method for signal integration,[28] the similar natures of the CH_2 carbon environments allow for the anhydride:en-MCM-41 ratio to be roughly estimated and give input on the structure of en-(COO^-)-MCM-41. The ^{13}C NMR spectrum of FSNs 6 (en-(COO^-)$_3$-MCM-41) (Figure 1c) shows the characteristic peaks of both carbons in $-SiCH_2CH_2-$ (Table S1). All the other CH_2 carbons appear in the 55−63 ppm region and are tentatively assigned based on the ^{13}C NMR data available for TANED in literature.[29] A single characteristic carbonyl ^{13}C peak is observed at 177 ppm and contains all the carboxylic acid environments within en-(COO^-)$_3$-MCM-41.

The monodispersity of FSNs 4 and FSNs 5 is confirmed by TEM and SEM (Figure 2). The FSNs maintain roughly pseudospherical shape and show negligible enlargement compared with native MCM-41 (Figure S2), as their diameters are narrowly distributed in the range of 70−90 nm. The TEM images (Figure 2a,c) reveal clearly that the two-dimensional hexagonal *p6mm* ordered mesopores are also intact after the functionalization. However, some larger particles 500−800 nm in length appeared (Figure S3) when native MCM-41 nanoparticles were treated with a higher dose of aqueous TANED solution (that results in FSNs 6). It is due to the high temperature instability of nanosized silica in the presence of water.[30,31]

The diameters of FSNs were also evaluated with dynamic light scattering (DLS), as shown in Table 1. Both FSNs 4 and FSNs 5 present high monodispersity in water suspensions, with number-weighted hydrodynamic diameter of 82 and 85 nm, respectively. The measured diameter (171.8 ± 2.8 nm) of FSNs 2, however, is bigger than the actual diameters found in the

DOI: 10.1021/acsami.5b08028
ACS Appl. Mater. Interfaces XXXX, XXX, XXX−XXX

Table 1. Structural Information Obtained from TGA, DLS, and N_2 Adsorption Results

functionalization	name	organic content (mmol/g)	ξ-size (nm)	ξ-potential (mv)	BET (m^2/g)	pore volume (cm^3/g)	pore size (nm)
	MCM-41	0	154.6 ± 12.5	−20.2 ± 1.5	1075	0.93	3.8
en-	FSNs 1	0.24 ± 0.06	170.0 ± 5.4	−17.2 ± 1.2	929	0.78	3.1
	FSNs 2	0.69 ± 0.11	171.8 ± 2.8	−15.2 ± 0.5	886	0.70	2.8
en-(COO^-)−	FSNs 3	0.22 ± 0.09	82.5 ± 8.0	−42.5 ± 4.8	856	0.72	2.8
	FSNs 4	0.66 ± 0.07	81.7 ± 6.4	−45.5 ± 0.3	806	0.67	2.5
en-(COO^-)$_3$−	FSNs 5	0.23 ± 0.04	85.3 ± 5.2	−45.3 ± 0.5	791	0.63	2.8
	FSNs 6	0.71 ± 0.20	192.8 ± 24.8	−49.5 ± 1.6	476	0.36	2.6

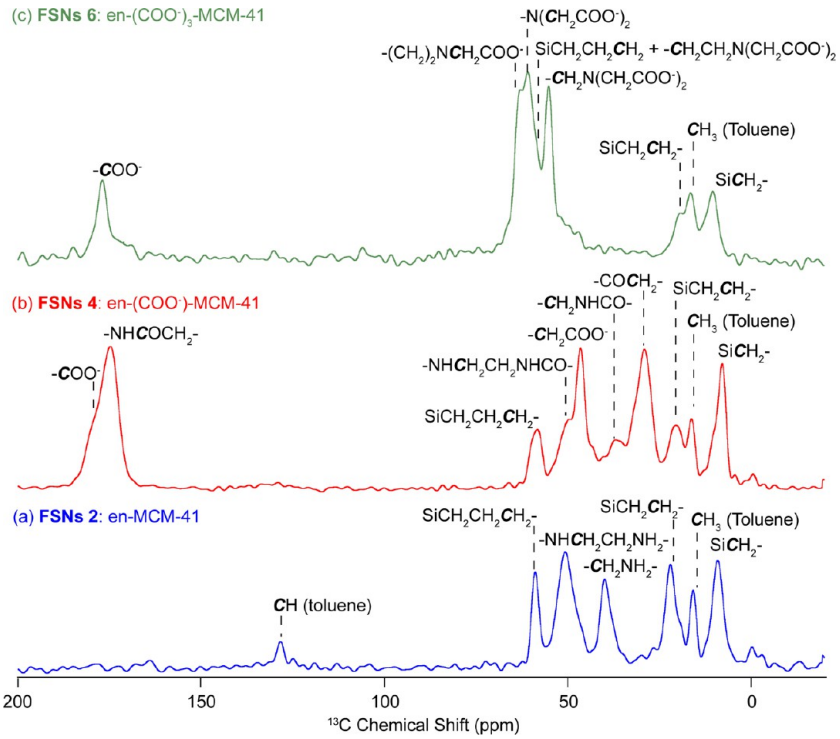

Figure 1. ^{13}C CP MAS NMR spectra of (a) FSNs 2, en-MCM-41; (b) FSNs 4, en-(COO^-)-MCM-41; and (c) FSNs 6, en-(COO^-)$_3$-MCM-41 materials at 0.7 mmol/g organic functionalization, obtained at 9.4 T. The spectral assignments are also given in the figure (see Table S1 for further details). Residual toluene physisorbed on the silica particles could be seen at 16 (CH_3) and 128 (Ar) ppm.

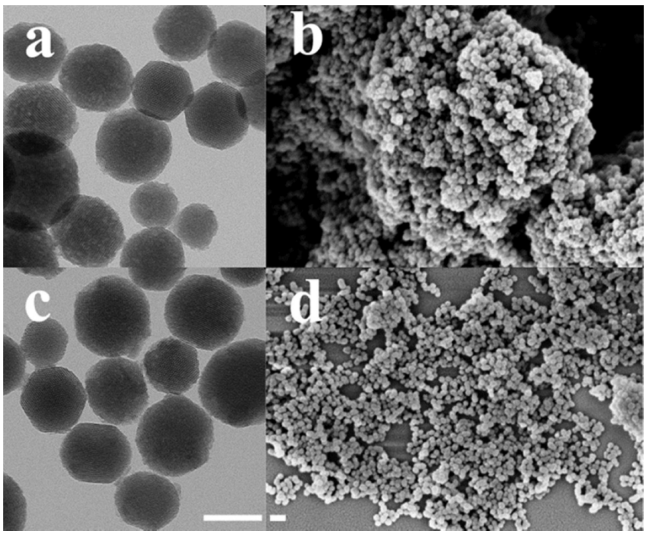

Figure 2. TEM and SEM images of (a and b) FSNs 4 and (c and d) FSNs 5. The analysis based on electron micrographs yields diameters around 70−90 nm. TEM scale bar: 100 nm. SEM scale bar: 200 nm.

electron micrographs, implying the presence of agglomerates. The ξ-potentials of these samples (Table 1) also confirm the functionalization and the DLS results. This is because the carboxylate-functionalized silica nanocontainers are so highly charged (about −45 mV) that the particles are well separated by electrostatic repulsion, while the ethylendiamine-covered samples are only negatively charged at −15 mV. The charge neutralization at silica surface induced by the functionalization of the diamine groups is believed to lead to an agglomeration of particles.

Figures 3 and S4 show small-angle X-ray scattering (SAXS) patterns of FSNs. In Figure 3, the native silica containers (curve I) exhibit well-resolved (100), (110) and (200) peaks at q = 1.7, 2.9, and 3.4 nm^{-1}, confirming a structure with hexagonal *p6mm* order. The high-dose functionalization with en and en-(COO^-) groups did not damage the regular structure because the scattering intensity and peak width of curve II and III remain similar to that of the bare one.[32] An extra shoulder at around 1.8 nm^{-1} reveals the partial shrinkage in diameter of the mesopores.[33] We have noticed this phenomenon in our previous work[34] where we have shown that the interior wall of the mesopores was easier modified by silyl agents with small molecular weight. Shrinkage is also plausible for materials with

DOI: 10.1021/acsami.5b08028
ACS Appl. Mater. Interfaces XXXX, XXX, XXX−XXX

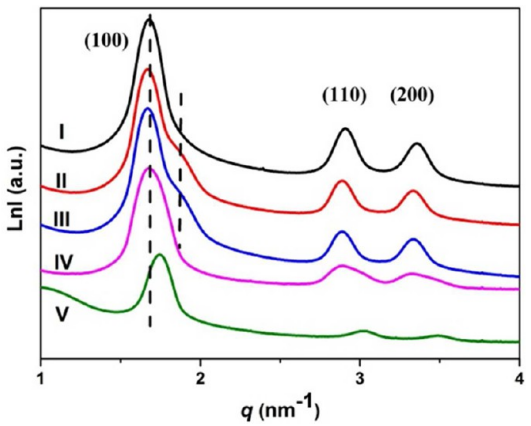

Figure 3. SAXS spectra of native MCM-41 (I), FSNs 2 (II), FSNs 4 (III), FSNs 5 (IV) and FSNs 6 (V). The peak at q = 1.7 nm^{-1} and shoulder peak at q = 1.85 nm^{-1} are indicated by dashed lines.

thin wall thickness, such as MCM-41 (1.6 nm).[35] Thus, the shoulder toward the higher q value is ascribed to the inner functionalization of FSNs. For en-$(COO^-)_3$-MCM-41, the regular mesoporous structure is preserved after a low-dose functionalization, because the (100) peak remains intact and the other two at higher q values can also be easily detected. FSNs 6 differs from this behavior since curve V shows three much weaker and broadened scattering peaks, which indicates the distortion of the regular mesoporous structure.

Inhibitor Loading and Release. The porosity of the native and functionalized silica nanocontainers was evaluated with N_2 sorption measurements and show a type IV isotherm for all samples analyzed (Figure 4a). The adsorption isotherms were analyzed by the nonlocal density functional theory (NLDFT) kernel for cylindrical silica pores.[36] The values of pore volume, Brunauer–Emmett–Teller (BET) surface area, and pore diameter D_{DFT} of the samples are given in Table 1. In Figure 4a native MCM-41 shows a sharp adsorption step at intermediate P/P_0 value (0.2–0.4), suggesting nitrogen condensation inside the mesopores by capillarity[37] and thus a potential capability for loading corrosion inhibitors. Upon functionalization, FSNs 2 and FSNs 4 obtain decreased values of the isotherm plateau, corresponding to the shrinkage in pore volume of ca. 25 and 30%, respectively. The partial functionalization on the inner wall of the mesopores found in both FSNs 2 and FSNs 4 is believed to reduce the loading capacity. Pore volume always plays a governing factor in the situation where high amounts of cargo molecules are required.[26] Thus, the theoretical uptake amount of cargo would be reduced upon the functionalization. In addition, the pore diameter of native MCM-41 witnessed a reduction by 1 nm after treatment with en groups (peak II, Figure 4b). It is further decreased to 2.5 nm after the further carboxylation (peak III).

FSNs 5 (curve IV, Figure 4a) exhibits a similar N_2 sorption isotherm as FSNs 4, with pore volume and S_{BET} being shrunk to 0.63 cm^3/g and 791 m^2/g, respectively. But it contrarily keeps a relatively large pore size which is narrowly distributed at around 2.8 nm (peak IV in Figure 4b). Combined with no evidence for inner deposition in Figure 3, we propose the en-$(COO^-)_3$ functionalization occurs exclusively at the orifice or the exterior surface of silica nanocontainers. FSNs 6 show an isotherm characteristic of nonporous materials (curve V in Figure 4a)

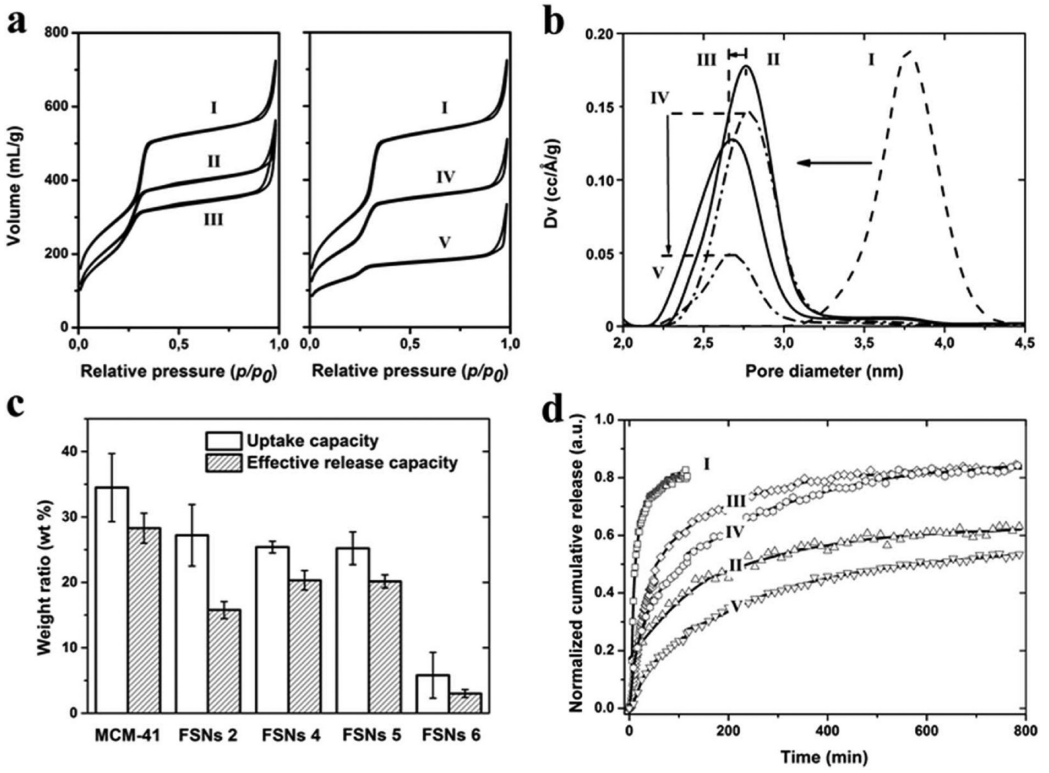

Figure 4. (a) Nitrogen sorption isotherms and (b) pore diameter distribution for native MCM-41 (I), FSNs 2 (II), FSNs 4 (III), FSNs 5 (IV) and FSNs 6 (V). (c) The uptake capacity and release capacity of these nanocontainers were analyzed by TGA and UV–vis spectroscopy, respectively. (d) The release profile of BTA from the loaded native MCM-41 (I), FSNs 2 (II), FSNs 4 (III), FSNs 5 (IV), and FSNs 6 (V) in neutral environment.

DOI: 10.1021/acsami.5b08028
ACS Appl. Mater. Interfaces XXXX, XXX, XXX–XXX

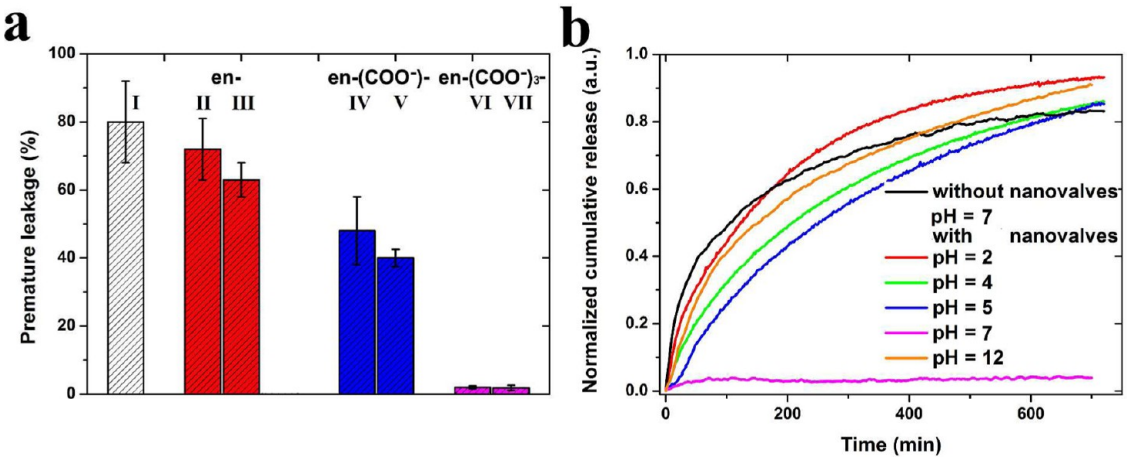

Figure 5. (a) Premature leakage of BTA from I (native MCM-41), II (FSNs 1), III (FSXNs 2), IV (FSNs 3), V (FSNs 4), VI (FSNs 5), and VII (FSNs 6) with Co-carbonate nanovalves. The data have been normalized by effective release capacity. (b) Release profiles of BTA from the C-L FSNs 5.

Table 2. Comparison of C-L FSNs in This Work with Other Products Reported Recently

products	container	stimuli-response	key compound	price (£/g)[a]	nanovalve strategy
mesoporous zirconia nanospheres	zirconia	H^+/OH^- dual response	zirconium(iv) butoxide	0.16	
			L-carnosine	8.58	
mechanized hollow mesoporous silica nanoparticle	silica		cucurbit-[7]uril	1500	supramolecular assembly
			ferrocenedicarboxylic acid	70	
C-L FSNs			TANED	1.2	direct spraying
			cobalt(II) nitrate hexahydrate	0.26	
			sodium carbonate	0.08	

[a]The prices of the key compounds are based on prices from the Sigma-Aldrich U.K. company.

due to the weak nitrogen condensation inside the mesopores. The change of sorption type together with the notable decrease of the pore volume (0.34 cm^3/g) and S_{BET} (476 m^2/g) confirm the collapse of the mesoporous structure. Furthermore, the sharp decrease of the capacity between peaks IV and V in Figure 4b also exclude FSNs 6 as a candidate of nanocontainers for loading inhibitor molecules.

As shown in Figure 4c, the native MCM-41 nanocontainers exhibit the highest BTA loading at 34.5 wt %, which agrees well with their largest pore volume among the analyzed samples. The uptake capacities are identical among FSNs 4 and FSNs 5, which are slightly lower than FSNs 2 (27.2 wt %). The weight ratio of BTA on FSNs 6 was found to be the lowest one at 5.8 wt %, which is mainly due to its lowest value of pore volume. At the same time, Figure 4c,d also unveil that the effective release capacity of FSNs 2 is only 60% of the loaded BTA. Its slow release rate indicates a notable interaction between diamine groups and guest molecules. Balas et al.[38] reported that strengthened interaction between the carboxylic acid (from ibuprofen) and the amine groups (from modified MCM-41) led to a slower ibuprofen release. In our work, the electrostatic attraction between negatively charged BTA^- (derived from dissociation of 1*H*-benzotriazole, pKa = 6.64)[39] and $-NH_3^+$ groups (on the inner wall and orifice of mesopores) retarded the release of cargo. The native MCM-41 and two other carboxylate functionalized silica nanocontainers (FSNs 4 and FSNs 5), on the contrary, can release 80% of the stored inhibitor molecules at higher release rates.

Stimuli-Induced Release of Inhibitor. The cobalt carbonates nanovalves were formed according to the method reported by us.[27] We compared the Co content of the capped and loaded (C-L) FSNs 4 and FSNs 5 (Figure S5) because they both presented relatively high uptake and release capacity. The result of energy-dispersive X-ray spectroscopy (EDX) shows that cobalt accounts for 1.7 wt % in C-L FSNs 5 while only 0.19 wt % in C-L FSNs 4. The role of en-$(COO^-)_3$ in stabilizing nanovalves can be a synergistic effect of chelation and steric blocking. We believe the chelating effect plays a dominant role, because Co^{2+} can form a stable complex with iminodiacetic acid with an formation constant of 10^7,[40] while the one for Co-carboxylate complexes is always below 1.[41] In agreement with the EDX result, C-L FSNs 5 (VI, Figure 5a) lead to the best performance in minimizing premature leakage to lower than 2%. For FSNs 4, a notable leakage of inhibitor at 40% was detected, indicating that even the high-dose en-(COO^-) groups cannot keep enough cobalt basic carbonates as nanovalves. For the other capped containers except FSNs 6 the premature leakages are all above 60% of the loaded amount.

Figure 5b confirms the negligible premature leakage of C-L FSNs 5 with a flat baseline at neutral environment. Furthermore, lowering pH value helps to accelerate the release of BTA. At the same time, increasing the pH value to 12 is unexpectedly found to stimulate the release of inhibitor as well. Analysis for pH-sensitive release is detailed in Supporting Information. Our pH sensitive nanocontainers are especially suitable for responsive anticorrosion applications because they provide rapid inhibitor release and protection in response to acidic as well as basic microenvironment. Besides, we compare C-L FSNs 5 with other two products recently reported[42,43] (Table 2) to emphasize that the en-$(COO^-)_3$− type

DOI: 10.1021/acsami.5b08028
ACS Appl. Mater. Interfaces XXXX, XXX, XXX−XXX

functionalization facilitates a cost-effective and simple way to form H^+/OH^-dual responsive nanovalves for the large-scale production.

Physical Properties of the Coating. In this study, a water-borne epoxy coating[11] was utilized as a passive coating host for C-L FSNs. The thickness of all the cured coatings deposited on the aluminum alloy was measured to be around 50 μm with a coating thickness gauge using the Eddy-current principle.[44] The representative SEM images depicting the cross sections of hybrid coatings containing free BTA, C-L FSNs 2, 4, and 5 are shown in Figure 6. Both the sample contains free

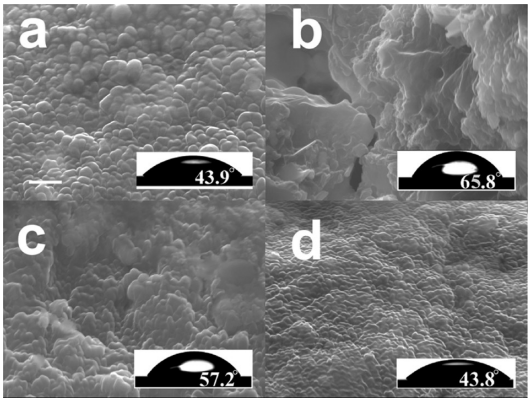

Figure 6. SEM images of cross-section of selected coatings incorporating (a) free BTA, C-L (b) FSNs 2, (c) FSNs 4, and (d) FSNs 5. (Insets) Drop images on the surface of silicon wafer functionalized with (a) nothing, (b) Co^{2+}-en complex, (c) Co^{2+}-en-(COO^-) complex, and (d) Co^{2+}-en-$(COO^-)_3$ complex. SEM scale bar: 1 μm.

corrosion inhibitor (Figure 6a) and C-L FSNs 5 (Figure 6d) appear with a uniformly and closely packed grainy structure. Although it is not possible to highlight the position and aggregation extent of the particles within the coating by SEM, the large aggregates or obvious crack were not observed. On the contrary, a large number of notable cracks, defects and fractures can be detected in the other samples, especially the one incorporating C-L FSNs 2. A possible poor distribution of the containers in the coating would lead to the formation of agglomerates, thus increasing the stress in the coating matrix.[11] It is well-known that epoxy/amine adduct reaction was widely utilized in epoxy coating to enhance mechanical behavior, promote adhesion and facilitate monodispersity of capsules in coating matrix.[45,46] Despite that amine groups on the surface of FSNs 2 may help increase the compatibility of the uncapped containers in water-borne coating matrix, C-L FSNs 2 show a poor distribution in coating matrix. To solve this problem, we mainly focused on the wettability of FSNs. It is difficult to measure the wettability of particles with diameter below 100 nm, thus we tested Si(100) surfaces which were functionalized with en-, en-$(COO^-)-$ or en-$(COO^-)_3-$ featured silyl moieties and then are further modified by incorporation of Co^{2+} ions (Supporting Information). In the experiment, we found that silicon wafers functionalized with en-$(COO^-)_3$ generally led to a contact angle around 30°, which can then be tuned to 43.8° by capturing cobalt ions from $Co(NO_3)_2$ solution (Figure 6d inset). The resulting hydrophobicity is close to that of the clean silicon wafer freshly obtained from pretreatment by piranha solution (Figure 6a inset). Differently, the wafer with en-(COO^-) functionalization shows a contact angle at 53° and a slightly larger one at 57.2° after incorporation of cobalt ions (Figure 6c inset). The en-modified wafer exhibits a similar contact angle as the pristine one, but the highest value (65.8°) can be obtained by chelating Co^{2+} with en groups, as shown in Figure 6b. On the basis of the above hydrophobicity measurement and SEM observation, we conclude that loaded FSNs 5 with cobalt carbonates nanovalves keep the best compatibility in the water-borne epoxy coating matrix. In addition, the surface morphologies of doped coating, revealed by top-view SEM (Figure S6), are also in agreement with our conclusion. The smoothest coating surface was obtained by introducing C-L FSNs 5 into the coating matrix, where the lowest roughness and no obvious cracks and bulges were detected.

Anticorrosive Properties of Coating. To further study the effectiveness of FSNs-based controlled release systems in hybrid coatings, we employe scanning vibrating electrode technique (SVET)d in a control experiment to detect the current flow caused by corrosion above the scratched area where the local pH shift has been experimentally proved.[47] The current density around a corrosion site can be calculated by converting electric field into an alternating voltage on a vibrating electrode whose resistance is already known. Thus, the measured current density over an area can be plotted as a 3D current density map. At the same time, a plot showing the current density as a function of time can be drawn by recording the minimum and maximum current densities over the scanned area. An increase in anodic current density reflects the dissolution of metal ions from the substrate due to ongoing corrosion.[48] The detected anodic current densities as a function of time for the coated AA2024-T3 aluminum alloy samples are shown in Figure S7. Except the pure epoxy coating, all samples exhibit obvious corrosion resistance and self-healing ability because all the anodic current densities were effectively suppressed at around 2 $\mu A/cm^2$. This behavior can be attributed to sufficiently high inhibitor concentration near the artificial defect. However, after putting the four freshly scratched samples in a flowing artificial seawater environment for 1 h to remove free or leaked inhibitors, the coatings containing free BTA as well as C-L FSNs 2 and 4 lost or weakened the ability of self-healing (Figure 7). The one hosting C-L FSNs 5, on the contrary, still maintained the suppression of anodic and cathodic currents. This constantly effective self-healing protection suggests that the inhibitor can be well preserved in capped FSNs 5 and be released when the local pH value is shifted. The controlled release system based on FSNs 5 can unquestionably prolong the serving time of self-healing anticorrosive coatings.

To investigate the impact of functionalization on self-healing performance, all coated samples were immersed in 1 M NaCl solution and anticorrosion performance of the coatings was analyzed with electrochemical impedance spectroscopy (EIS) over a time range of 49 days. First of all, we compared the impedance modules at the lowest frequency ($|Z|_{0.01\ Hz}$) of Bode plots acting as a measure for the corrosion resistance of the respective coating.[13,14] Figure 8a shows a general impedance decrease of the samples containing free BTA, C-L FSNs 2 and 4. The degradation of the protective coatings advances with an increase of immersion time. However, the sample containing FSNs 5 exhibits a recovery of impedance after a drop at the initial stage. Until the end of immersion, the $|Z|_{0.01\ Hz}$ value of $5.28 \times 10^5\ \Omega\ cm^2$ is even higher than the one at the first day. In Figure 8c, the optical photographs of the coated samples after 7

DOI: 10.1021/acsami.5b08028
ACS Appl. Mater. Interfaces XXXX, XXX, XXX−XXX

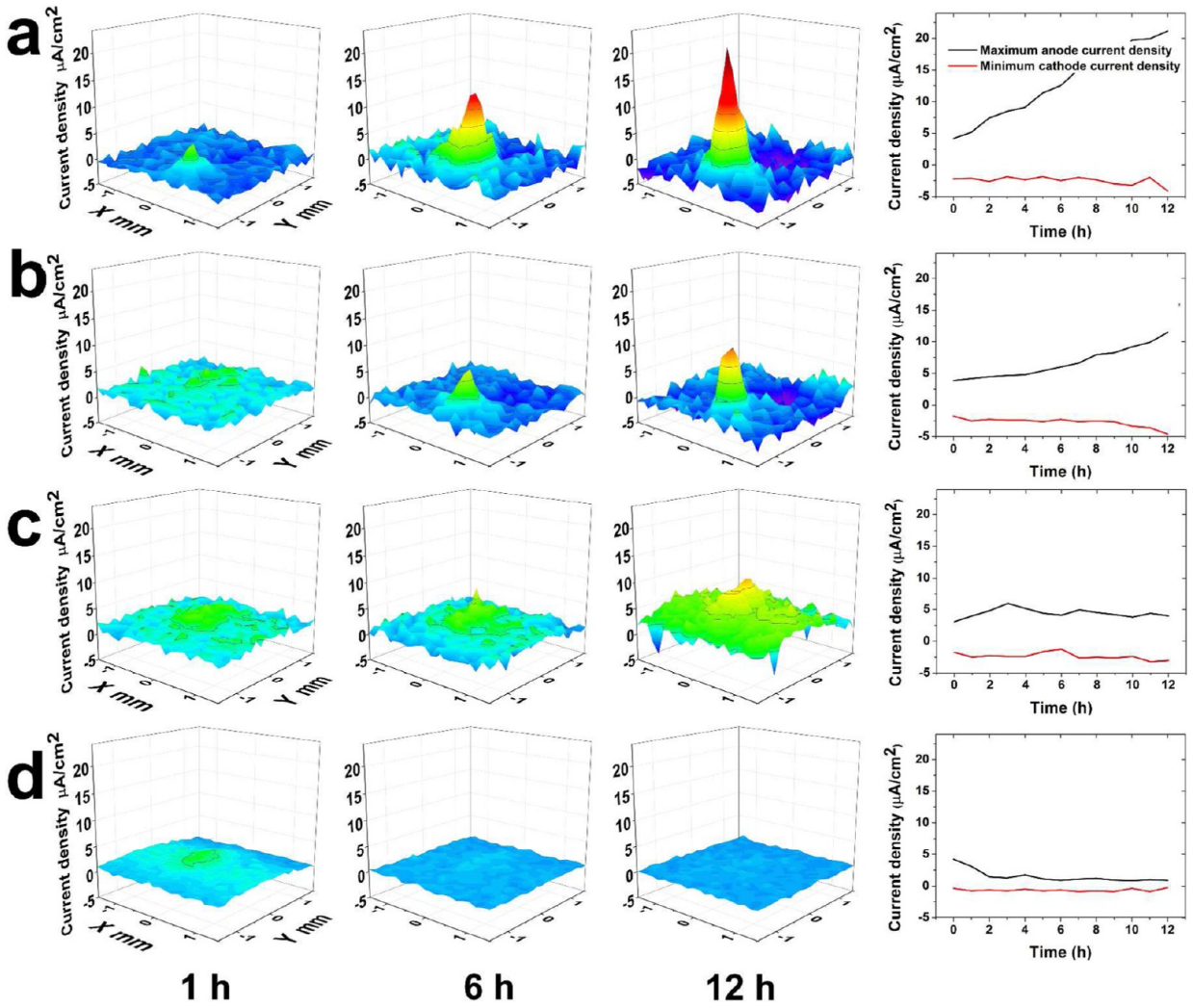

Figure 7. SVET 3D current density maps of aluminum (AA2024-T3) substrates coated with an epoxy coating containing (a) free inhibitor, C-L (b) FSNs 2, (c) FSNs 4, and (d) FSNs 5. The measurement was conducted at 1, 6, and 12 h after prewash with a flowing artificial seawater environment for 1 h to remove free or leaked inhibitors. Right: Maximum anodic and minimum cathodic current densities detected with SVET over the scanned scratched area during a 12 h immersion period in 0.1 M NaCl.

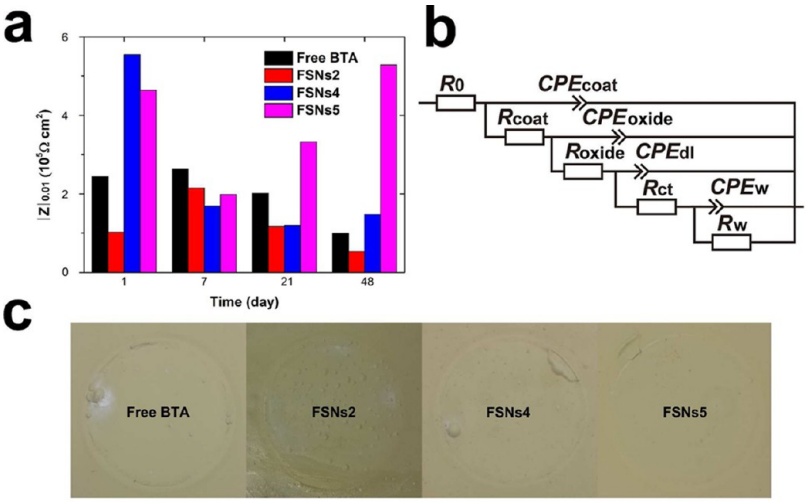

Figure 8. (a) Impedance modulus |Z| measured at 0.01 Hz during 49 days immersion in 1 M NaCl for coatings with free BTA and C-L FSNs 2, 4, and 5. (b) The equivalent circuit used to fit the EIS spectra obtained during the 49 days of immersion in 1 M NaCl. (c) Optical photographs of the coated samples after 7 weeks of immersion in 1 M NaCl.

DOI: 10.1021/acsami.5b08028
ACS Appl. Mater. Interfaces XXXX, XXX, XXX−XXX

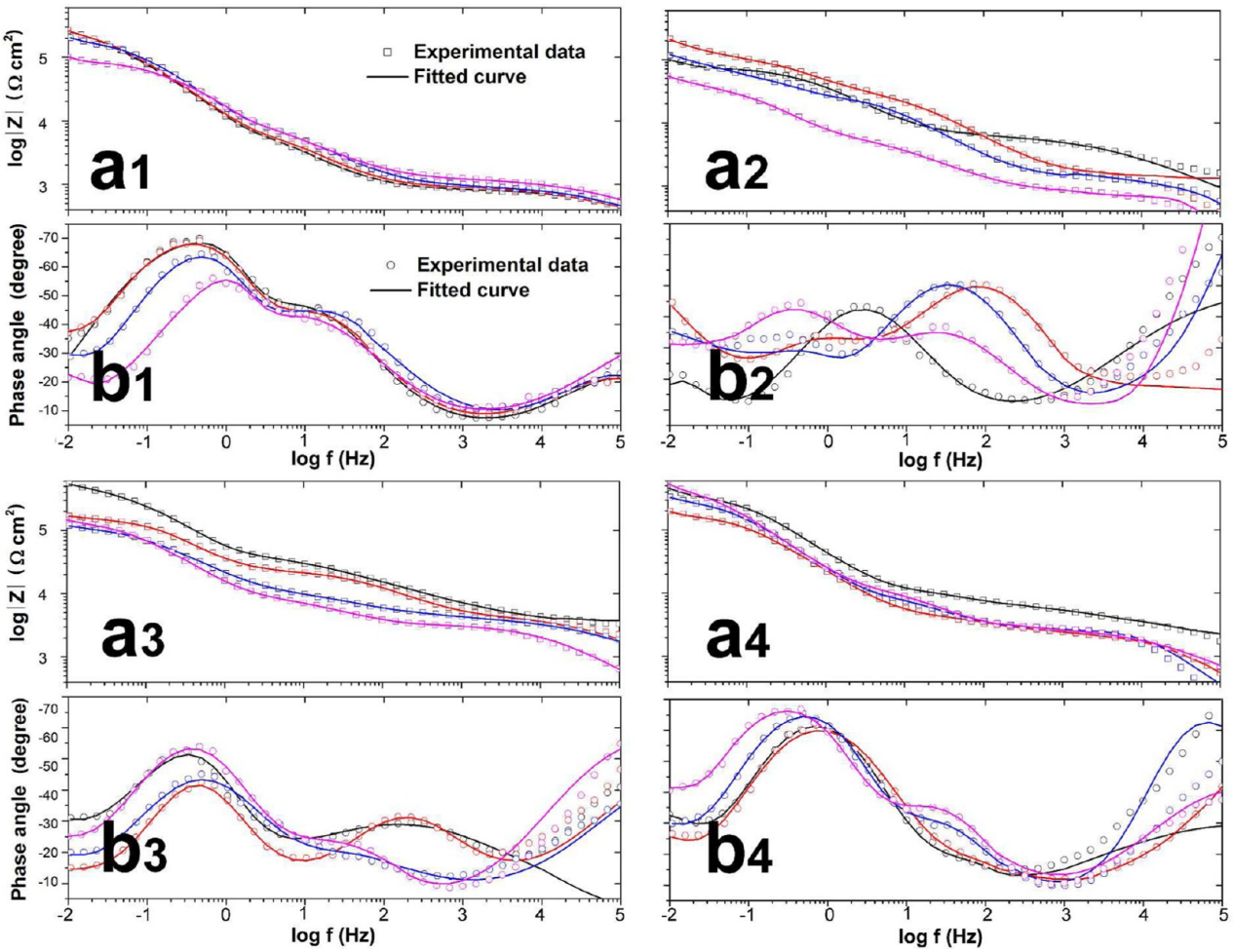

Figure 9. Bode plots showing the absolute impedance (a_1, a_2, a_3, and a_4) and phase angle (b_1, b_2, b_3, and b_4) as a function of frequency after 49 days immersion in 1 M NaCl of AA2024-T3 aluminum alloy substrates coated with organic coatings containing free BTA, C-L FSNs 2, FSNs 4, and FSNs 5, respectively. The experimental data was collected after (black) 1, (red) 7, (blue) 21, and (magenta) 49 immersion days.

weeks immersion in 1 M NaCl are in agreement with the $|Z|_{0.01\ Hz}$ result. The coating with C-L FSNs 5 is strikingly different from other samples because no coating cracks, deposits of white corrosion products or delamination were observed on the surface.

The Bode plots of coated samples during 7 immersion weeks in 1 M NaCl are represented in Figure 9. We chose an equivalent circuit in Figure 8b to describe the electrochemical response of the relaxation processes occurring in the coated samples. The fitting model delivers a good fit quality ($\chi^2 < 0.01$) and contains all reasonable resistive and capacitive contributions in the coating systems, for example, coating response (CPE_{coat} and R_{coat} at 10^4–10^5 Hz), aluminum oxide layer response (CPE_{oxide} and R_{oxide} at 10–10^3 Hz), elements describing occurrence of corrosion (CPE_{dl} and R_{ct} at 10^{-1} to 1 Hz) and ones describing the mass transport (CPE_w and R_w at 10^{-2} Hz). Here, the constant phase elements (CPE) were used instead of capacitances to account for the dispersive character of the time constants originating from the nonuniformity of the layers.[49] The true capacitance will be calculated using the equation proposed elsewhere.[50]

The obtained fitting parameters for the coating response are depicted in Figure S8. With increased immersion time, the corrosive species gradually penetrate the cracks or pores of the coatings, resulting in the decrease of impedance modulus of all samples, reflecting the weakened passive barrier effect. The coating containing C-L FSNs 5 exhibits a higher R_{coat} value as compared with the other samples, indicating that low agglomeration tendency and high dispersibility of the nanocontainers in the coating matrix help to reduce diffusion pathways for aggressive electrolyte and slower degradation of coatings.

Aluminum oxide layer is a natural protective layer against corrosion. The resistive element of oxide layers (R_{oxide}) appears when the electrolyte can penetrate through forming conductive pathways.[51] The evolution of R_{oxide} values with time is a very important indicator for evaluating the ability of self-healing, since the repair factors formed between inhibitor and copper ions[10] can gradually compensate the damaged oxide layer and prevent the further propagation of conductive pathways. Figure 10a shows the coating containing free BTA has a half cut in R_{oxide} value after 7 immersion weeks. R_{oxide} of the samples doped with C-L FSNs 2 and 4 drop fast as well and achieve only $0.6 \times 10^4\ \Omega\ cm^2$ in the last 6 weeks. In strong contrast, the coating with C-L FSNs 5 exhibits a stable resistance increase from 0.6 to $1.4 \times 10^4\ \Omega\ cm^2$ during 49 immersion days. This behavior can be explained in terms of prolonged release of corrosion inhibitor. Figure 10c shows that the corresponding oxide capacitance has also been maintained at a relatively low value (1.2×10^{-6} F cm^{-2}).

DOI: 10.1021/acsami.5b08028
ACS Appl. Mater. Interfaces XXXX, XXX, XXX−XXX

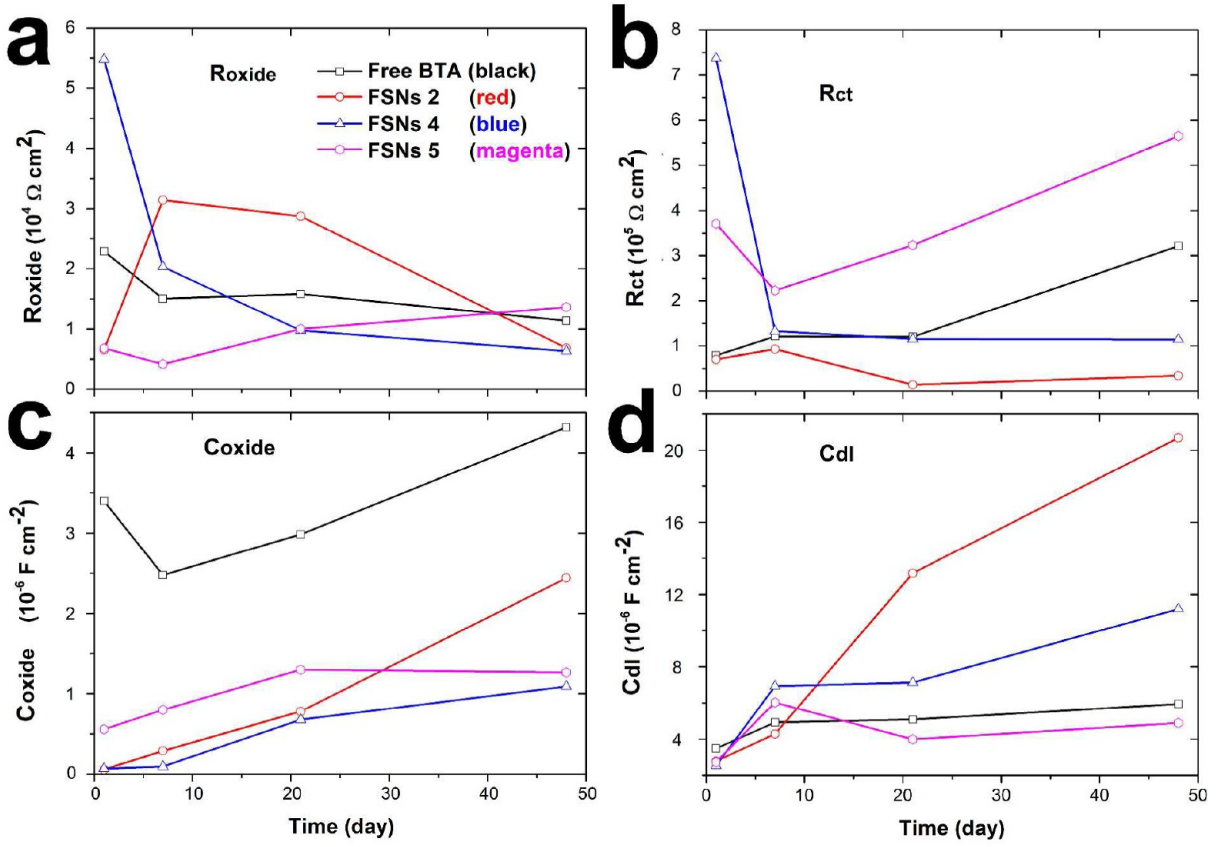

Figure 10. Calculated data for the (a) oxide resistance (R_{oxide}), (b) charge transfer resistance (R_{ct}), (c) oxide capacitance (C_{oxide}), and (d) double layer capacitance (C_{dl}) obtained by fitting of the EIS spectra using the equivalent circuit shown in Figure 8b.

R_{ct} reflects the kinetics of the electrochemical reactions at the interface and is directly dependent on the effects of self-healing. Accordingly, the gradual rising trend and the highest R_{ct} value (5.8×10^5 Ω cm^2) at the end of immersion for the coating containing C-L FSNs 5 can be due to the effective controlled release of inhibitor and self-healing protection for a long serving time (Figure 10b). The double layer capacitance (C_{dl}), on the other hand, is directly related to the metal area exposed to the electrolyte, therefore providing information about the wet adhesion of the coating to the metal. A high C_{dl} value always accounts for a high extent of corrosion and a high degree of coating degradation or worse adhesion of the coating to the metal surface. The highest C_{dl} value (21×10^{-6} F cm^{-2}) for the coating containing C-L FSNs 2 is consistent with lowest R_{ct} value (0.34×10^5 Ω cm^2) among all samples and severe pit-like defects shown in Figure 8c. For the coating doped with C-L FSNs 5, the lowest value of C_{dl} after 7 immersion weeks can be attributed to good adhesion of the coating to the metal surface and suppressed corrosion evolution by self-healing ability of the coating. Overall, the EIS study confirms the better anticorrosive performance of the coating containing C-L FSNs 5 which is compatible with the coating matrix, effective to preserve inhibitor and respond to the corrosion-induced pH change.

CONCLUSIONS

Nanocontainer-based coating serves as a solution for the challenge of self-healing for corrosion processes. Comprehensive consideration of the factors including the uptake and release capacity of containers, prevention of premature release, compatibility of nanocontainers in the coating matrix and low cost allows one to optimize the self-healing performance-to-cost ratio by tailoring the type and content of functionalization of nanocontainers. In this work, the en-$(COO-)_3$-type functionalization with a content of 0.23 mmol/g was shown to be the best option for self-healing anticorrosive performances of hybrid coatings. By incorporating the fabricated nanocontainers into the coating, the further occurrence of corrosion is suppressed by the long-term self-healing effect derived from the high inhibitor uptake and release capacity and response to local pH change resulted from corrosion. We believe the success in this systematic work would pave the way for excellent designs in the field of self-healing materials and facilitate the rational consideration about how to establish a multifunctional coating.

ASSOCIATED CONTENT

Supporting Information

The Supporting Information is available free of charge on the ACS Publications website at DOI: 10.1021/acsami.5b08028.

Experimental details (materials and reagents, synthetic procedure, loading procedure, formation of nanovalves, surface functionalization of silicon wafers, coatings procedure, structure characterization and analysis for pH sensitive release), ^{13}C chemical information, TEM, TGA data, SAXS pattern and HAADF-STEM image for FSN samples, SEM images of surface morphology of hybrid coatings, time-dependent maximum anodic current and coating resistance evolutions with immersion time. (PDF)

DOI: 10.1021/acsami.5b08028
ACS Appl. Mater. Interfaces XXXX, XXX, XXX−XXX

AUTHOR INFORMATION

Corresponding Author

*E-mail: zhaoliang.zheng@liverpool.ac.uk.

Notes

The authors declare no competing financial interest.

ACKNOWLEDGMENTS

This work was financially supported by the ERC ENER-CAPSULE grant, the Brian Mercer Feasibility Award of the Royal Society of Chemistry, the University of Liverpool and the EPSRC (EP/M00869X/1). N.J.B. thanks the EPSRC for a DTA studentship.

REFERENCES

(1) Shchukin, D.; Möhwald, H. A Coat of Many Functions. *Science* **2013**, *341*, 1458−1459.

(2) Davis, J. R., Ed. *Corrosion: Understanding the Basics*; ASM International: Materials Park, OH, 2000.

(3) Zheludkevich, M. L.; Serra, R.; Montemor, M. F.; Salvado, I. M. M.; Ferreira, M. G. S. Corrosion Protective Properties of Nano-structured Sol-Gel Hybrid Coatings to AA2024-T3. *Surf. Coat. Technol.* **2006**, *200*, 3084−3094.

(4) Shukla, P. G.: Microencapsulation of Liquid Active Agents. In *Functional Coatings*; Wiley-VCH Verlag GmbH & Co. KGaA: Weinheim, 2006, 153−186.

(5) White, S. R.; Sottos, N. R.; Geubelle, P. H.; Moore, J. S.; Kessler, M. R.; Sriram, S. R.; Brown, E. N.; Viswanathan, S. Autonomic Healing of Polymer Composites. *Nature* **2001**, *409*, 794−797.

(6) Latnikova, A.; Grigoriev, D. O.; Hartmann, J.; Mohwald, H.; Shchukin, D. G. Polyfunctional Active Coatings with Damage-Triggered Water-Repelling Effect. *Soft Matter* **2011**, *7*, 369−372.

(7) Grigoriev, D. O.; Kohler, K.; Skorb, E.; Shchukin, D. G.; Mohwald, H. Polyelectrolyte Complexes as A "Smart" Depot for Self-Healing Anticorrosion Coatings. *Soft Matter* **2009**, *5*, 1426−1432.

(8) Skorb, E. V.; Fix, D.; Andreeva, D. V.; Mohwald, H.; Shchukin, D. G. Surface-Modified Mesoporous SiO2 Containers for Corrosion Protection. *Adv. Funct. Mater.* **2009**, *19*, 2373−2379.

(9) Haase, M. F.; Grigoriev, D. O.; Mohwald, H.; Shchukin, D. G. Development of Nanoparticle Stabilized Polymer Nanocontainers with High Content of the Encapsulated Active Agent and Their Application in Water-Borne Anticorrosive Coatings. *Adv. Mater.* **2012**, *24*, 2429−2435.

(10) Latnikova, A.; Grigoriev, D.; Schenderlein, M.; Mohwald, H.; Shchukin, D. A New Approach Towards "Active" Self-Healing Coatings: Exploitation of Microgels. *Soft Matter* **2012**, *8*, 10837−10844.

(11) Borisova, D.; Akçakayıran, D.; Schenderlein, M.; Möhwald, H.; Shchukin, D. G. Nanocontainer-Based Anticorrosive Coatings: Effect of the Container Size on the Self-Healing Performance. *Adv. Funct. Mater.* **2013**, *23*, 3799−3812.

(12) Borisova, D.; Mohwald, H.; Shchukin, D. G. Mesoporous Silica Nanoparticles for Active Corrosion Protection. *ACS Nano* **2011**, *5*, 1939−1946.

(13) Borisova, D.; Moehwald, H.; Shchukin, D. G. Influence of Embedded Nanocontainers on the Efficiency of Active Anticorrosive Coatings for Aluminum Alloys Part I: Influence of Nanocontainer Concentration. *ACS Appl. Mater. Interfaces* **2012**, *4*, 2931−2939.

(14) Borisova, D.; Moehwald, H.; Shchukin, D. G. Influence of Embedded Nanocontainers on the Efficiency of Active Anticorrosive Coatings for Aluminum Alloys Part II: Influence of Nanocontainer Position. *ACS Appl. Mater. Interfaces* **2013**, *5*, 80−87.

(15) Snihirova, D.; Lamaka, S. V.; Taryba, M.; Salak, A. N.; Kallip, S.; Zheludkevich, M. L.; Ferreira, M. G. S.; Montemor, M. F. Hydroxyapatite Microparticles as Feedback-Active Reservoirs of Corrosion Inhibitors. *ACS Appl. Mater. Interfaces* **2010**, *2*, 3011−3022.

(16) Jafari, A. H.; Hosseini, S. M. A.; Jamalizadeh, E. Investigation of Smart Nanocapsules Containing Inhibitors for Corrosion Protection of Copper. *Electrochim. Acta* **2010**, *55*, 9004−9009.

(17) Joshi, A.; Abdullayev, E.; Vasiliev, A.; Volkova, O.; Lvov, Y. Interfacial Modification of Clay Nanotubes for the Sustained Release of Corrosion Inhibitors. *Langmuir* **2013**, *29*, 7439−7448.

(18) Boyle, M. M.; Smaldone, R. A.; Whalley, A. C.; Ambrogio, M. W.; Botros, Y. Y.; Stoddart, J. F. Mechanised materials. *Chem. Sci.* **2011**, *2*, 204−210.

(19) Angelos, S.; Khashab, N. M.; Yang, Y.-W.; Trabolsi, A.; Khatib, H. A.; Stoddart, J. F.; Zink, J. I. pH Clock-Operated Mechanized Nanoparticles. *J. Am. Chem. Soc.* **2009**, *131*, 12912−12914.

(20) Angelos, S.; Yang, Y.-W.; Khashab, N. M.; Stoddart, J. F.; Zink, J. I. Dual-Controlled Nanoparticles Exhibiting AND Logic. *J. Am. Chem. Soc.* **2009**, *131*, 11344−11346.

(21) Du, L.; Liao, S.; Khatib, H. A.; Stoddart, J. F.; Zink, J. I. Controlled-Access Hollow Mechanized Silica Nanocontainers. *J. Am. Chem. Soc.* **2009**, *131*, 15136−15142.

(22) Zhao, Y.-L.; Li, Z.; Kabehie, S.; Botros, Y. Y.; Stoddart, J. F.; Zink, J. I. pH-Operated Nanopistons on the Surfaces of Mesoporous Silica Nanoparticles. *J. Am. Chem. Soc.* **2010**, *132*, 13016−13025.

(23) Xue, M.; Zhong, X.; Shaposhnik, Z.; Qu, Y.; Tamanoi, F.; Duan, X.; Zink, J. I. pH-Operated Mechanized Porous Silicon Nanoparticles. *J. Am. Chem. Soc.* **2011**, *133*, 8798−8801.

(24) Muhammad, F.; Guo, M.; Qi, W.; Sun, F.; Wang, A.; Guo, Y.; Zhu, G. pH-Triggered Controlled Drug Release from Mesoporous Silica Nanoparticles via Intracelluar Dissolution of ZnO Nanolids. *J. Am. Chem. Soc.* **2011**, *133*, 8778−8781.

(25) Manzano, M.; Colilla, M.; Vallet-Regi, M. Drug Delivery from Ordered Mesoporous Matrices. *Expert Opin. Drug Delivery* **2009**, *6*, 1383−1400.

(26) Manzano, M.; Vallet-Regi, M. New Developments in Ordered Mesoporous Materials for Drug Delivery. *J. Mater. Chem.* **2010**, *20*, 5593−5604.

(27) Zheng, Z.; Huang, X.; Shchukin, D. A Cost-Effective pH-Sensitive Release System for Water Source pH Detection. *Chem. Commun.* **2014**, *50*, 13936−13939.

(28) Laws, D. D.; Bitter, H.-M. L.; Jerschow, A. Solid-State NMR Spectroscopic Methods in Chemistry. *Angew. Chem., Int. Ed.* **2002**, *41*, 3096−3129.

(29) Bronstein, L. M.; Linton, C.; Karlinsey, R.; Stein, B.; Timofeeva, G. I.; Svergun, D. I.; Konarev, P. I.; Kozin, M.; Tomaszewski, J.; Werner-Zwanziger, U.; Zwanziger, J. W. Functional Polymer Colloids with Ordered Interior. *Langmuir* **2004**, *20*, 1100−1110.

(30) Chen, L. Y.; Jaenicke, S.; Chuah, G. K. Thermal and Hydrothermal Stability of Framework-Substituted MCM-41 Mesoporous Materials. *Microporous Mater.* **1997**, *12*, 323−330.

(31) Kim, J. M.; Kwak, J. H.; Jun, S.; Ryoo, R. Ion-Exchange and Thermal-Stability of Mcm-41. *J. Phys. Chem.* **1995**, *99*, 16742−16747.

(32) Kónya, Z.; Puntes, V. F.; Kiricsi, I.; Zhu, J.; Ager, J. W.; Ko, M. K.; Frei, H.; Alivisatos, P.; Somorjai, G. A. Synthetic Insertion of Gold Nanoparticles into Mesoporous Silica. *Chem. Mater.* **2003**, *15*, 1242−1248.

(33) Huang, E.; Toney, M. F.; Volksen, W.; Mecerreyes, D.; Brock, P.; Kim, H.-C.; Hawker, C. J.; Hedrick, J. L.; Lee, V. Y.; Magbitang, T.; Miller, R. D.; Lurio, L. B. Pore Size Distributions in Nanoporous Methyl Silsesquioxane Films as Determined by Small Angle X-Ray Scattering. *Appl. Phys. Lett.* **2002**, *81*, 2232−2234.

(34) Zheng, Z.; Huang, X.; Schenderlein, M.; Borisova, D.; Cao, R.; Möhwald, H.; Shchukin, D. Self-Healing and Antifouling Multifunctional Coatings Based on pH and Sulfide Ion Sensitive Nanocontainers. *Adv. Funct. Mater.* **2013**, *23*, 3307−3314.

(35) Akcakayiran, D.; Kurth, D. G.; Röhrs, S.; Rupprechter, G.; Findenegg, G. H. Self-Assembly of a Metallosupramolecular Coordination Polyelectrolyte in the Pores of SBA-15 and MCM-41 Silica. *Langmuir* **2005**, *21*, 7501−7506.

(36) Ravikovitch, P. I.; Wei, D.; Chueh, W. T.; Haller, G. L.; Neimark, A. V. Evaluation of Pore Structure Parameters of MCM-41

DOI: 10.1021/acsami.5b08028
ACS Appl. Mater. Interfaces XXXX, XXX, XXX−XXX

Catalyst Supports and Catalysts by Means of Nitrogen and Argon Adsorption. *J. Phys. Chem. B* **1997**, *101*, 3671−3679.
(37) Agostini, A.; Mondragon, L.; Pascual, L.; Aznar, E.; Coll, C.; Martinez-Manez, R.; Sancenon, F.; Soto, J.; Marcos, M. D.; Amoros, P.; Costero, A. M.; Parra, M.; Gil, S. Design of Enzyme-Mediated Controlled Release Systems Based on Silica Mesoporous Supports Capped with Ester-Glycol Groups. *Langmuir* **2012**, *28*, 14766−14776.
(38) Balas, F.; Manzano, M.; Colilla, M.; Vallet-Regi, M. L-Trp Adsorption Into Silica Mesoporous Materials to Promote Bone Formation. *Acta Biomater.* **2008**, *4*, 514−522.
(39) Li, Y.; Gong, M.; Ramji, K.; Li, Y. Role of Cu−Benzotriazole Nanoparticles in Passivation Film Formation. *J. Phys. Chem. C* **2009**, *113*, 18003−18013.
(40) Schwarzenbach, G.; Anderegg, G.; Schneider, W.; Senn, H. Komplexone XXVI. Über die Koordinationstendenz von N-substituierten Iminodiessigsäuren. *Helv. Chim. Acta* **1955**, *38*, 1147−1170.
(41) Bunting, J. W.; Thong, K. M. Stability Constants for Some 1:1 Metal−Carboxylate Complexes. *Can. J. Chem.* **1970**, *48*, 1654−1656.
(42) Wang, M.; Liu, M.; Fu, J. An Intelligent Anticorrosion Coating Based on pH-Responsive Smart Nanocontainers Fabricated via a Facile Method for Protection of Carbon Steel. *J. Mater. Chem. A* **2015**, *3*, 6423−6431.
(43) Fu, J.; Chen, T.; Wang, M.; Yang, N.; Li, S.; Wang, Y.; Liu, X. Acid and Alkaline Dual Stimuli-Responsive Mechanized Hollow Mesoporous Silica Nanoparticles as Smart Nanocontainers for Intelligent Anticorrosion Coatings. *ACS Nano* **2013**, *7*, 11397−11408.
(44) Kral, J.; Smid, R.; Ramos, H. G. presented at *Instrumentation and Measurement Technology Conference (12MTC)*, 2011, IEEE 10−12 May 2011, 2011.
(45) Huang, T.; Lu, R. G.; Su, C.; Wang, H. N.; Guo, Z.; Liu, P.; Huang, Z. Y.; Chen, H. M.; Li, T. S. Chemically Modified Graphene/Polyimide Composite Films Based on Utilization of Covalent Bonding and Oriented Distribution. *ACS Appl. Mater. Interfaces* **2012**, *4*, 2699−2708.
(46) Lim, J.; Yeo, H.; Goh, M.; Ku, B. C.; Kim, S. G.; Lee, H. S.; Park, B.; You, N. H. Grafting of Polyimide onto Chemically-Functionalized Graphene Nanosheets for Mechanically-Strong Barrier Membranes. *Chem. Mater.* **2015**, *27*, 2040−2047.
(47) Fix, D.; Skorb, E. V.; Shchukin, D. G.; Mohwald, H. Quantitative Analysis of Scanning Electric Current Density and pH-value Observations in Corrosion Studies. *Meas. Sci. Technol.* **2011**, *22*, 22.
(48) He, J.; Gelling, V. J.; Tallman, D. E.; Bierwagen, G. P. A Scanning Vibrating Electrode Study of Chromated-Epoxy Primer on Steel and Aluminum. *J. Electrochem. Soc.* **2000**, *147*, 3661−3666.
(49) Amand, S.; Musiani, M.; Orazem, M. E.; Pebere, N.; Tribollet, B.; Vivier, V. Constant-Phase-Element Behavior Caused by Inhomogeneous Water Uptake in Anti-corrosion Coatings. *Electrochim. Acta* **2013**, *87*, 693−700.
(50) Hsu, C. H.; Mansfeld, F. Technical note: Concerning the Conversion of the Constant Phase Element Parameter Y-0 into a Capacitance. *Corrosion* **2001**, *57*, 747−748.
(51) Zheludkevich, M. L.; Serra, R.; Montemor, M. F.; Yasakau, K. A.; Salvado, I. M. M.; Ferreira, M. G. S. Nanostructured Sol−Gel Coatings Doped with Cerium Nitrate as Pre-treatments for AA2024-T3: Corrosion Protection Performance. *Electrochim. Acta* **2005**, *51*, 208−217.

DOI: 10.1021/acsami.5b08028
ACS Appl. Mater. Interfaces XXXX, XXX, XXX−XXX